nature communications

Article

https://doi.org/10.1038/s41467-026-74250-2

Efficient preservation of old methane-derived organic carbon in deep-sea surface sediments

Received: 9 October 2024

Accepted: 3 June 2026

Published online: 17 June 2026

Check for updates

Rui Bao[1,2,12] ✉, Yangli Che[1,2,12], Mingzhi Liu[1,2,12], Naiyu Zhang[3,12], Yang Zhou[4,12], Lihua Dong[1,2,12], Shen Li[1,2], Owen A. Sherwood[5], Min Yu[6], Zongheng Chen[4], Shengxiong Yang[7], Nan Wang[8], Longhai Zhu[8], Jiawang Chen[9], Mutai Bao[1,2], Haoshuai Li[1,2], Luonan Chen[10], Weifeng Wu[1,2], Haiyue Ma[1,2] & David J. Burdige[11]

Methane released from the subseafloor is significantly attenuated during upward migration, yet the preservation of methane-derived organic carbon (OC) in global deep-sea sediments remains poorly understood. Here, we measured carbon isotopes coupled with temperature-ramped analyses on various methane seepage sediments. Our results reveal a correlation between the radiocarbon (^{14}C) content in deep-sea surface sediments and sulfate-methane transition depth. Notably, our findings suggest that a substantial amount of ^{14}C-depleted OC may originate from deep-seated methane and is efficiently preserved in surface seepage sediments. We propose that the efficient OC preservation is related to microbial-mediated aggregate formation at the seawater-sediment interface, where physical occlusion within coarse-grained matrices reduces oxygen availability and enhances OC stability. We estimate that at least 6 Tg C of methane-derived OC are preserved annually in surface sediments of the global continental slopes. This process may play a non-negligible role in OC preservation in sediments, reducing methane emission into the atmosphere.

Methane is a potent greenhouse gas with a warming potential approximately 28 times relative to carbon dioxide over a 100-year timescale[1,2]. Substantial amounts of methane are trapped in ice-like solid hydrates in subseafloor sediments[2–4]. There is evidence that methane from the subseafloor can be released into the atmosphere, which is thought to be a non-negligible driving factor of rising surface temperature on Earth[5,6]. The decomposition of hydrates results in the generation and upward emission of methane gas. In situ underwater observations in the deep sea have revealed the visible release of methane bubbles from the seabed sediments into seawater[7,8]. It is therefore essential to investigate the processes of seafloor methane emissions and their transformation products.

[1]Frontiers Science Center for Deep Ocean Multispheres and Earth System, Key Laboratory of Marine Chemistry Theory and Technology, Innovation Center for Ocean Carbon Neutrality, Ocean University of China, Qingdao, China. [2]Laboratory for Marine Geology, Qingdao Marine Science and Technology Center, Qingdao, China. [3]State Key Laboratory of Estuarine and Coastal Research, East China Normal University, Shanghai, China. [4]Guangzhou Marine Geological Survey, China Geological Survey, Guangzhou, China. [5]Department of Earth and Environmental Sciences, Dalhousie University, Halifax, Canada. [6]College of Marine Life Sciences, Ocean University of China, Qingdao, China. [7]Southern Marine Science and Engineering Guangdong Laboratory, Guangzhou, China. [8]Frontiers Science Center for Deep Ocean Multispheres and Earth System, Key Lab of Submarine Geosciences and Prospecting Techniques, Ministry of Education and College of Marine Geosciences, Ocean University of China, Qingdao, China. [9]Donghai Laboratory, Zhoushan, China. [10]School of Mathematical Sciences, Shanghai Jiao Tong University, Shanghai, China. [11]Department of Ocean and Earth Sciences, Old Dominion University, Norfolk, USA. [12]These authors contributed equally: Rui Bao, Yangli Che, Mingzhi Liu, Naiyu Zhang, Yang Zhou, Lihua Dong. ✉e-mail: baorui@ouc.edu.cn

Methane emitted from subseafloor sediments serves as an energy source for microbial communities, driving a cascade of biogeochemical processes within seafloor ecosystems. A substantial portion of this methane is consequently consumed and microbially transformed in marine sediments[4,9,10]. This microbial-mediated transformation can lead to the incorporation of methane carbon into organic matter[11], and the subsequent preservation of this methane-derived organic carbon (OC) in sediments. The methane-derived OC may constitute a potentially important carbon pool with implications for climate change. Its transformation and preservation are directly relevant to the regulation of methane emissions.

Central to these processes is the methane that migrates from deeper geological layers, yet its upward flux is predominantly controlled by sulfate-coupled anaerobic oxidation occurring within the sulfate-methane transition (SMT) zone[12,13]. Consequently, the depth of the SMT serves as a vital indicator of the potential for methane to reach the surface seabed. Methane emissions appear to be widespread across various marine sedimentary environments[14,15]. However, the extent to which methane-derived OC is preserved in marine sediments in relation to variations in SMT depth remains inadequately characterized on a broader spatial scale. This represents a significant knowledge gap in our understanding of methane cycling and its ultimate fate as a greenhouse gas.

Quantifying the preservation of OC derived from methane transformation across the vast seafloor remains challenging. Cold seeps, as extreme oceanic environments with high methane fluxes[16], offer natural settings to isolate the role of methane transformation in OC preservation within marine sediments. Moreover, observations of intermittent methane emissions from the seafloor suggest that methane continues to migrate across the sediment–water interface over extensive areas[14,15]. Therefore, cold seeps serve as critical windows for investigating the mechanisms and extent of methane-derived OC preservation.

The surface sediment layer acts as a critical control point, regulating benthic methane release and serving as the final barrier preventing seafloor methane from entering the water column[13]. Investigating methane transformation in surface seep sediments is therefore essential—not only for understanding methane-driven OC preservation, but also for assessing whether this carbon pool may ultimately contribute to atmospheric methane. This knowledge gap is particularly evident in deep-sea cold seep systems, which act as "distributed micro-valves" modulating global seabed methane emissions. However, limited attention has been paid to the quantitative contribution and preservation efficiency of methane-derived OC in marine surface seepage sediments, particularly regarding its impact on global OC sequestration.

In this study, we employ machine learning in conjunction with statistical analysis to investigate the potential global prevalence of methane-converted OC. To further elucidate the mechanisms underlying the preservation of methane-converted OC, we examine sediments collected from extreme environments of methane seepage in a series of cold seep habitats located in the northern South China Sea, where significant methane release from underlying sediments has been documented[16,17]. Temperature-ramped analyses, alongside stable and radiocarbon isotope measurements ($\delta^{13}C$ and $\Delta^{14}C$), are conducted on bulk and specific-grain-size sediments to identify and estimate the contribution of methane. Finally, we focus specifically on surface sediments, assessing the activation energy of OC and organo-mineral associations across different grain size fractions to explore the key processes governing the preservation of methane-derived OC.

Results and Discussion

Global prevalence of methane-derived OC preservation

To assess the global impact of methane transformation on OC burial, we compile literature data on global SMT depths, OC contents, and $\Delta^{14}C$ values in marine surface sediments. Based on these datasets, we generate global distribution maps and perform regression analyses (Fig. 1a–c). We find the increased OC contents and negative $\Delta^{14}C$ signatures in surface sediments with SMT depth decreases (Fig. 1d–f). Given that methane derived from subseafloor is of ancient origin (old ^{14}C age, depleted in ^{14}C)[18], this negative $\Delta^{14}C$ bias with shallowing SMT depth points to the incorporation of methane-derived carbon into deep-sea surface sedimentary OC.

Furthermore, the increased OC content shown in Fig. 1e implies that methane transformation contributes not only ^{14}C-old carbon but also additional OC burial in surface sediments. These results may provide independent evidence for the contribution of deep-sourced ancient methane-derived carbon to the deep-sea surface sediments, suggesting that the upward migration of the methane barrier enhances OC burial. On a global scale, methane migrating upward from deep sediments may thus represent an important component of the OC pool in surface marine sediments, shaping both its content and ^{14}C isotopic composition.

Given that the preservation of deep-sourced methane-derived OC in surface sediments appears to be a worldwide phenomenon, our finding may provide a unified explanation for the ubiquitous observation of elevated OC contents and aged ^{14}C ages in marine surface sediments, whose features are traditionally attributed primarily to terrestrial inputs and reworked marine OC[19]. Our results suggest that methane-derived OC burial may exert far-reaching influences on global scales, including in regions where active methane seepage is not detectable, yet this phenomenon is more pronounced at active seep sites. The methane transformation and OC preservation thus likely represent a pervasive process operating across the seafloor with varying intensities.

In this context, cold seeps with intensive methane emissions, often underlain by dissociating hydrates that release ^{14}C-depleted ("^{14}C-dead") methane[18], represent end-member environments where methane-derived carbon contributions are most pronounced. Given their global distribution and high emission fluxes, seepage systems warrant particular attention when assessing the role of methane-derived OC in marine carbon cycling.

More ^{14}C-depleted carbon signatures in seepage top sediments

To further investigate the signatures of methane-derived OC preservation in deep-sea extreme systems, we collect push cores from six distinct benthic seepage habitats in the South China Sea using a remotely operated vehicle (ROV) and analyze carbon isotopic compositions. These cores encompass a range of typical cold seep settings: sediments colonized by mussels around active methane seeps (Fig. 2c1–d1, sites #02 and #15), sediments covered by bacterial mats (Fig. 2a1–b1, sites #04 and #07), sediments adjacent to authigenic carbonate precipitates, and those covered by dead mussel shells (Fig. 2e1–f1, sites #06 and #05). These habitats represent different development stages of methane seepage (active, developmental, and recessional stages, respectively), providing a natural chronosequence to examine how methane-derived OC preservation evolves over the lifespan of a seep system.

We find that the most pronounced methane signals occur at sites #02 and #15, where surface sediments exhibit the highest OC contents (> 2.0%) and the most depleted $\Delta^{14}C$ values (the oldest ^{14}C ages: 9970 ± 50 and 9200 ± 40 yr BP) among all samples (Fig. 2c2–d2). These $\Delta^{14}C$ values are substantially more negative than those of marine sinking particulate OC (POC) in the South China Sea ($\Delta^{14}C$ values > −600‰ and ^{14}C ages <7000 yr)[20], indicating a significant contribution of ancient methane-derived carbon. In contrast, sediments from developmental and recessional stages show relatively consistent or slightly decreasing OC contents with depth, accompanied by a progressive downcore decline in $\Delta^{14}C$ values (Fig. 2a2–b2, e2–f2), which is consistent with steady depositional conditions and OC

https://doi.org/10.1038/s41467-026-74250-2

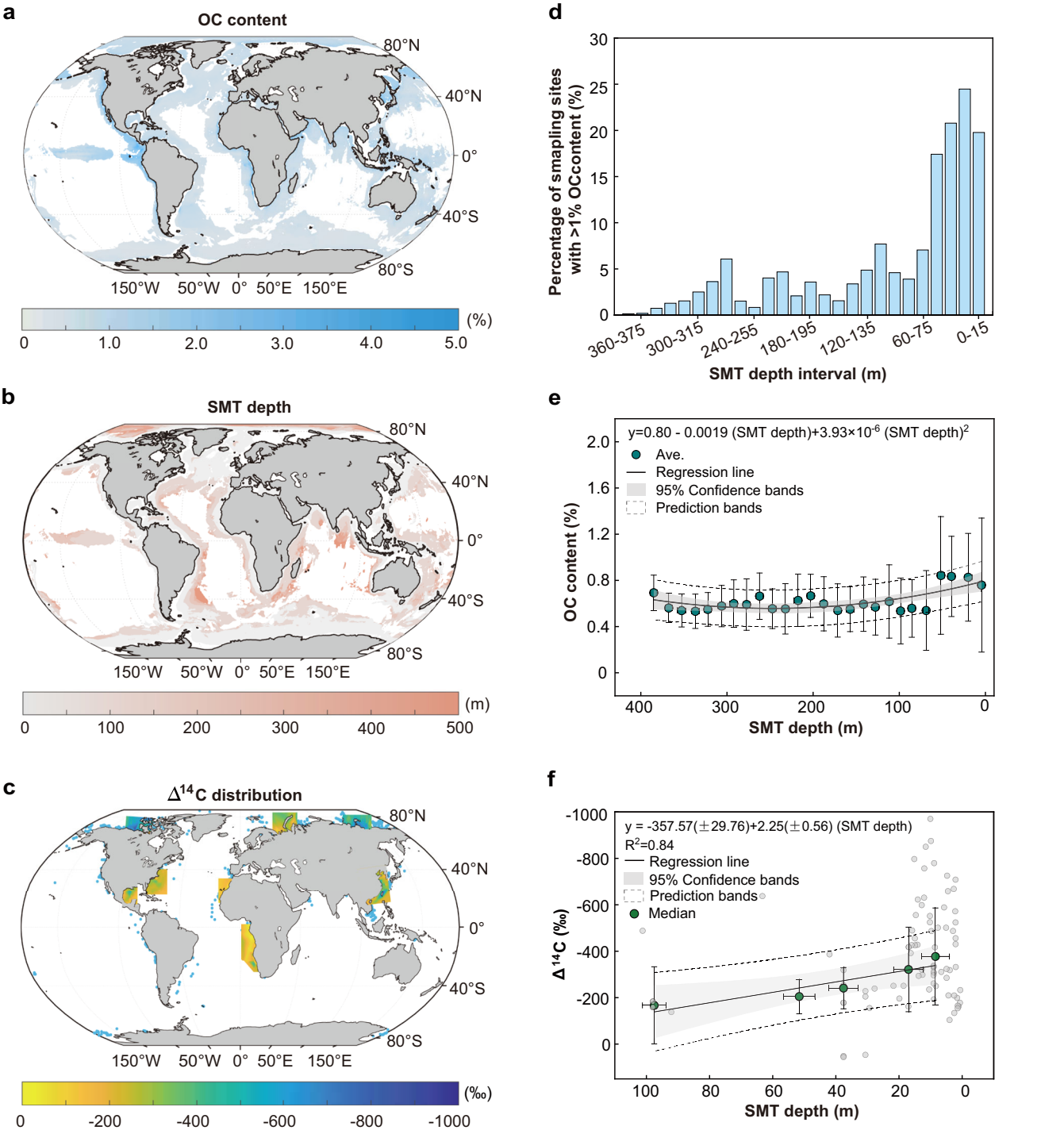


Fig. 1 | Global distributions and relationships between organic carbon (OC) characteristics of surface marine sediments and sulfate-methane transition (SMT) depth. a Global distribution of modeled OC contents in surface sediments (0.25° × 0.25° resolution). **b** Estimated SMT depth (0.25° × 0.25° resolution). **c** Available $\Delta^{14}C$ values of OC in surface sediments. **d** Distribution of percentage of sampling sites with OC contents >1% in each 15-m SMT depth interval. **e** Averaged OC content in each 15-m SMT depth interval. **f** $\Delta^{14}C$ values of OC against corresponding SMT depths. Green dots denote the median $\Delta^{14}C$ value of OC in each 15-m SMT depth interval (See Methods for model details and Supplementary Datasets 1–5 for all data).

degradation in non-extreme deep-sea sediments[21]. Notably, while $\Delta^{14}C$ generally decreases with depth in these non-active stages, the most depleted values at active methane seepage stages appear in surface sediments rather than deeper layers. These evidence further underscores the role of active methane emission in delivering ^{14}C-depleted carbon to the seafloor surface.

Building on this evidence, our findings further reveal that the incorporation of methane-derived OC into surface sediments is dynamically linked to the evolution of methane emissions, specifically, to the intensity and history of methane emissions. Methane ascending from deeper sediments is characterized by near-dead ^{14}C signatures ($\Delta^{14}C \approx -999‰$)[18], and its transformation into OC is most pronounced

https://doi.org/10.1038/s41467-026-74250-2

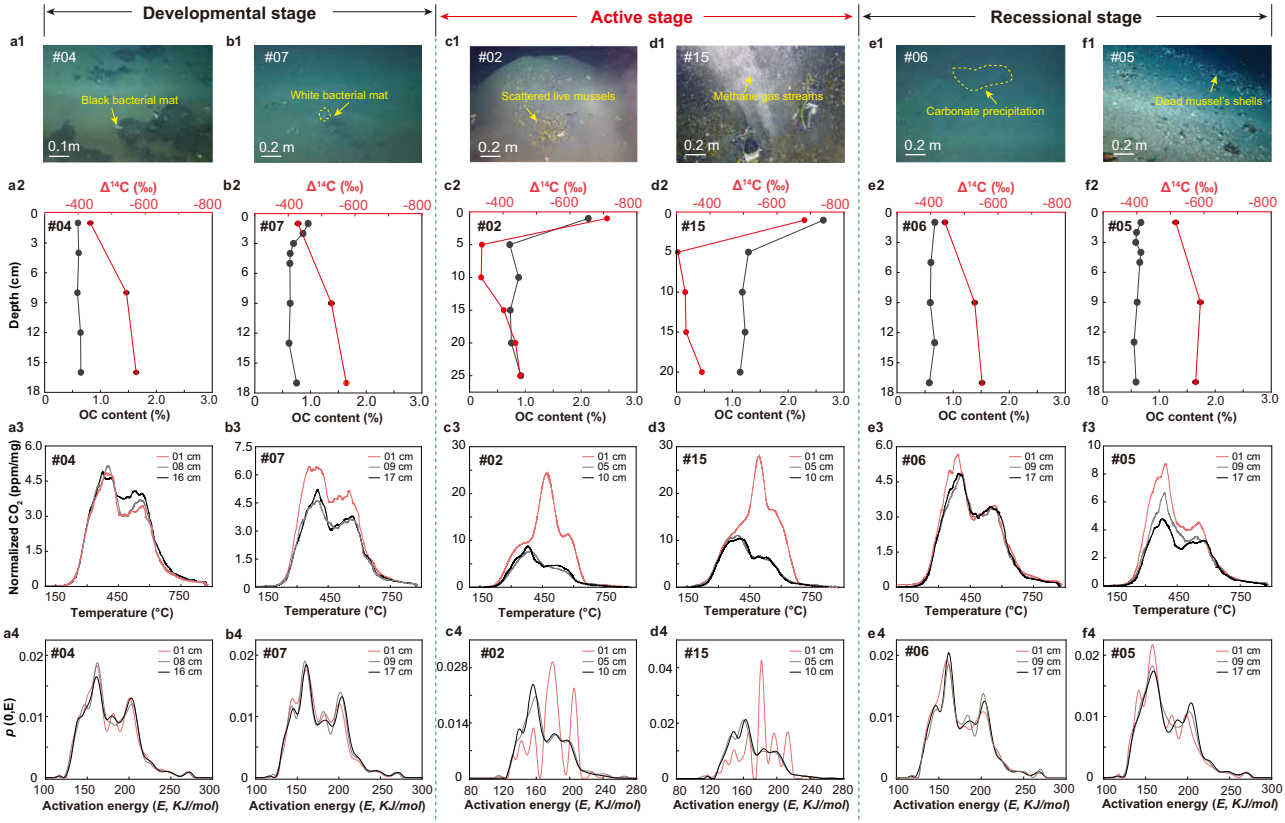


Fig. 2 | Biogeochemical fingerprints and thermal decomposition characteristics of OC from six cold seep habitats' sediments. a1 – f1 Photographs showing three types of seafloor scenes at cold seep regions: Developmental stage of methane seepage (#04, **a1** and #07, **b1**): their surface sediments are covered with dark and white bacterial mats, representing the colonization and accumulation of immense biomass; Active stage of methane seepage (#02, **c1** and #15, **d1**): sparse mussels are scattered in the seafloor sediments and dense mussel beds are distributed around the intense methane gas streams, respectively; Recessional stage of methane seepage (#06, **e1** and #05, **f1**): extensive carbonate blocks are exposed on the seafloor and abundant shells of dead mussels accumulate on the seafloor, respectively. **a2 – f2** Depth profiles of the contents and $\Delta^{14}C$ values of sedimentary OC. Red symbols denote $\Delta^{14}C$ values. **a3 – f3** Carbon dioxide (CO_2) thermograms of organic matter. Red lines denote thermograms of organic matter in the surface sediments. **a4 – f4** Activation energy distributions are shown below each thermogram. The X-axis indicates the activation energy (E) of organic matter decomposition, representing the energy required to break the chemical bonds of the compounds. The Y-axis is a probability density function on E (See Methods).

at active methane seepage stages, where surface sediments exhibit the strongest ^{14}C depletion and highest OC contents (Fig. 2c2–d2). In contrast, sediments from recessional stages show markedly lower OC contents and $\Delta^{14}C$ values that are substantially less depleted, indicating that the methane-derived carbon signal is largely absent once active seepage ceases. This stark contrast between active and non-active stages points to a critical distinction: the efficient preservation of methane-derived OC is not a ubiquitous feature of cold seeps, but rather a phenomenon tightly coupled to intensive methane seepage. Understanding the mechanisms that facilitate enhanced preservation during intensive methane seepage is crucial. Such insights may be pivotal in deciphering the often subtle and challenging-to-detect imprint of methane-derived OC preservation on a global scale.

Methane-derived OC preservation in the surface sediments

Elucidating the preservation mechanisms of methane-derived OC will advance our understanding of how seafloor methane emissions modulate the marine carbon cycle and potentially drive climate feedbacks on geological timescales. Here, we employ ramped pyrolysis/oxidation (RPO) to characterize the thermogram patterns and activation energy distributions of OC in those sediments. Our results reveal that intensive methane seepage sites (sites #02 and #15) exhibit distinct carbon dioxide (CO_2) thermograms (Fig. 2c3–d3), and activation energy distributions (Fig. 2c4–d4), compared to other sites. Specifically, the surface sediments (1 cm) from sites #02 and #15 show a pronounced high-temperature CO_2 peak that is absent in deeper layers, suggesting a greater abundance of refractory organic matter components and higher thermal activation energy in the surface carbon pool. In contrast, the thermogram shapes and activation energy patterns at developmental (sites #04, #07) and recessional (sites #06, #05) stages remain largely invariant with sediment depth. These results imply that active methane seepage not only delivers ancient carbon to the surface sediments but also facilitates the preferential preservation of methane-derived OC in a more refractory form, likely enhancing its potential for long-term burial in surface sediments.

We decompose the CO_2 thermograms from surface sediments of different methane seepage stages using a Gaussian distribution model (F1, F2, F3; Fig. 3a). The thermograms from developmental (sites #04, #07) and recessional (sites #06, #05) stages can be deconvolved into three components centered at 370 °C (F1), 550 °C (F2), and 750 °C (F3; Fig. 3a). In contrast, active stages (sites #02, #15) exhibit a distinct thermogram characterized by a sharp peak centered at 480 °C (Fig. 3a). The contribution of high-temperature OC components ($P_{CH4\text{-}C} = (F2 + F3)/(F1 + F2 + F3) \times 100\%$) is substantially larger at active sites than at other sites, coinciding with the oldest bulk OC ^{14}C ages observed in their surface sediments (Fig. 3b), which indicates that the methane-derived OC preserved in intensive methane seepage sediments is composed of refractory, energy-intensive forms that require higher thermal energy for degradation. Collectively, our results reveal a coherent link between CO_2 thermogram patterns and OC ^{14}C ages

https://doi.org/10.1038/s41467-026-74250-2

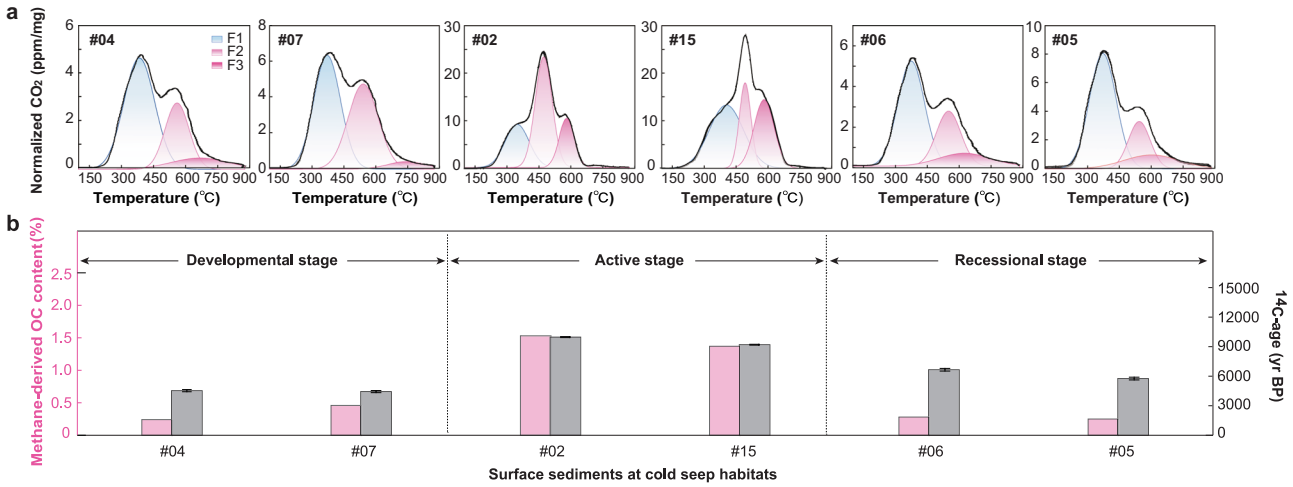


Fig. 3 | Gaussian decompositions of thermal fractions in sedimentary OC and the correlations of geochemical signatures at the surface sediments of six sites. **a** Distributions of thermal components (F1, F2, F3) based on Gaussian modeling decomposition. **b** Methane-derived OC content in sediments (rose-red bars, Methane-derived OC content %= OC content % × $P_{CH4\text{-}C}$) evaluated by the Gaussian model and ^{14}C ages of OC (gray bars) in surface sediments from the six sites.

across methane seepage evolutionary stages, suggesting that the enhanced preservation efficiency of methane-derived OC, particularly during active seepage, is tightly coupled to the intensity of ancient methane fixation in surface sediments. These findings demonstrate that active methane emission not only delivers ancient carbon to the seafloor but also promotes its selective preservation in a form resistant to diagenetic alteration.

We further employ RPO coupled with in-depth carbon isotopic analyses both on the surface (1 cm) and deeper (5 cm) sediments at active methane seepage sites (Fig. 4). Our results show that the $\delta^{13}C$ values of each thermal fraction (T1-5) in surface sediments (from −21.0‰ to −26.6‰) are significantly more negative than those in deeper sediments (from −20.1‰ to −23.8‰, Fig. 4a, b). In addition, lower $\Delta^{14}C$ values of each thermal fraction also appear in the surface sediments rather than in the deeper layer (Fig. 4a, b). These isotopic signatures of the thermal intervals from deep to surface sediments converge towards the methane end-member (Fig. 4c, arrow), demonstrating the presence and accumulation of methane-derived OC in surface sediments. This finding is also consistent with ^{14}C analyses of bulk sediments (Fig. 3b).

Furthermore, the most depleted $\Delta^{14}C$ signatures in surface sediments occur in the higher-temperature CO_2 fractions (T3–T5; Fig. 4a, b), which correspond to the F2 + F3 Gaussian components (Fig. 3a). As the higher-temperature CO_2 release is typically linked to more refractory organic matter[22], the association between $\Delta^{14}C$ signatures and higher-temperature CO_2 fractions indicates not only the incorporation of ancient methane-derived carbon, but also its stable preservation in surface sediments. Quantitative estimations based on ^{14}C mass balance reveal that methane-derived carbon accounts for 63% and 59% of the OC in surface sediments at the intensive methane seepage sites (#02 and #15), respectively, substantially higher than in deeper intervals (14% to 10%; Supplementary Table 1). These calculated proportions (mean 61 ± 2%) at sites #02 and #15 are consistent with those independently derived from Gaussian decomposition ($P_{CH4\text{-}C}$ = 62 ± 10%), corroborating that the F2 + F3 components (high-temperature components) are dominated by methane-derived OC (Fig. 3a). Together, these thermochemical and isotopic evidence demonstrate that methane-derived OC accumulating in surface sediments of intensive methane seepage regions has both ancient and refractory properties that confer enhanced preservation potential and underlie its efficient retention at the seafloor.

Grain size-specific preservation of methane-derived OC

To disentangle the influence of grain size on OC preservation, we measure RPO and the isotopic compositions of OC across different grain size fractions at active sites #02 and #15 (See Methods). RPO thermograms of the different grain-size fractions reveal a distinct pattern: surface sediments (1 cm) are dominated by high-temperature peaks, whereas deeper sediments (5 cm) exhibit flattened distributions, particularly in the coarse fraction (63–250 μm and >250 μm; Fig. 5a, b). Compared to fine fractions, the enhanced thermochemical stability and higher activation energy of coarse fractions (Supplementary Fig. 1), indicate that methane-derived OC is predominantly preserved in coarse fractions with a more refractory form. This inherently higher resistance to degradation[23,24], likely favors long-term preservation of methane-derived OC in surface sediments. In the meantime, the coarse fractions in surface sediments exhibit the highest OC contents (Supplementary Fig. 2). This pattern contrasts with typical marine sediments, where fine fractions generally host higher OC content[25]. Notably, these coarse fractions also display the most depleted $\delta^{13}C$ and $\Delta^{14}C$ values, which are substantially lower than those in deeper layers (Fig. 5c, d), suggesting preferential accumulation of methane-derived OC in coarse fractions in the surface sediment.

In aerobic surface sediments, methanotrophic communities assimilate methane for growth, producing biomass and microbial by-products that adhere to mineral surfaces[26,27]. While microbial-derived carbon may be conventionally regarded as a relatively labile fraction, its incorporation into coarse sediments can enhance long-term preservation of methane-derived OC. Critically, the surface enrichment of ancient carbon (Fig. 2c2–d2), is strongly associated with aerobic methanotrophs (function gene: *pmoA*) rather than anaerobic methanotrophs (function gene: *mcrA*; Supplementary Fig. 3), implicating aerobic methane oxidation (AeOM) as the important driver of surface OC accumulation. Aerobic methanotrophs assimilate methane-derived carbon at faster rates than their anaerobic counterparts[28], efficiently converting it into biomass that contributes directly to sedimentary OC. In contrast, anaerobic methanotrophs are slow growers[10], with most transformed methane carbon partitioned into inorganic pools. This functional divergence is reflected in gene abundances: *mcrA* represents only 1.2% and 38.5% of *pmoA* abundance in surface sediments at sites #02 and #15, respectively (Supplementary Fig. 3). This microbial activity may promote the agglomeration of sediment particles into coarse-grained aggregates.

https://doi.org/10.1038/s41467-026-74250-2

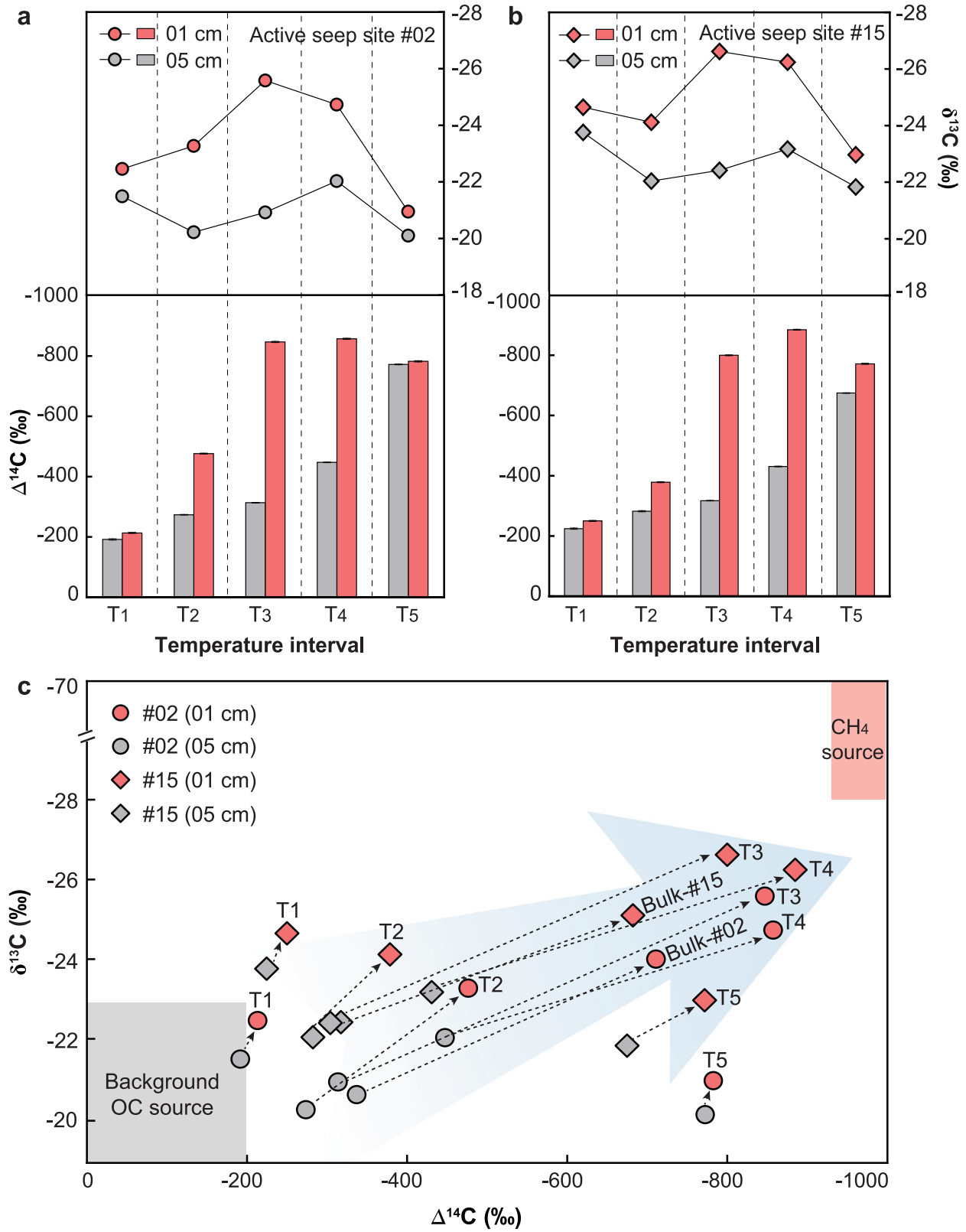


Fig. 4 | Carbon isotopic compositions of different thermal fractions at active seep sites. a, **b** $\delta^{13}C$ and $\Delta^{14}C$ values of pyrolysis components from the surface (1 cm) and deep (5 cm) sediments. The CO_2 thermograms of sediments are decomposed into five temperature intervals from T1 to T5 (T1: 80–320 °C; T2: 320–391 °C; T3: 391–484 °C; T4: 484–570 °C; T5: 570–900 °C). **c** Crossplot of $\delta^{13}C$ and $\Delta^{14}C$ values showing that the isotopic values of surface sediments tend to move towards the methane source, while deeper sediments tend towards the background marine OC source. The end-member values of the background marine OC and the methane source are shown[18,20,42,68].

https://doi.org/10.1038/s41467-026-74250-2

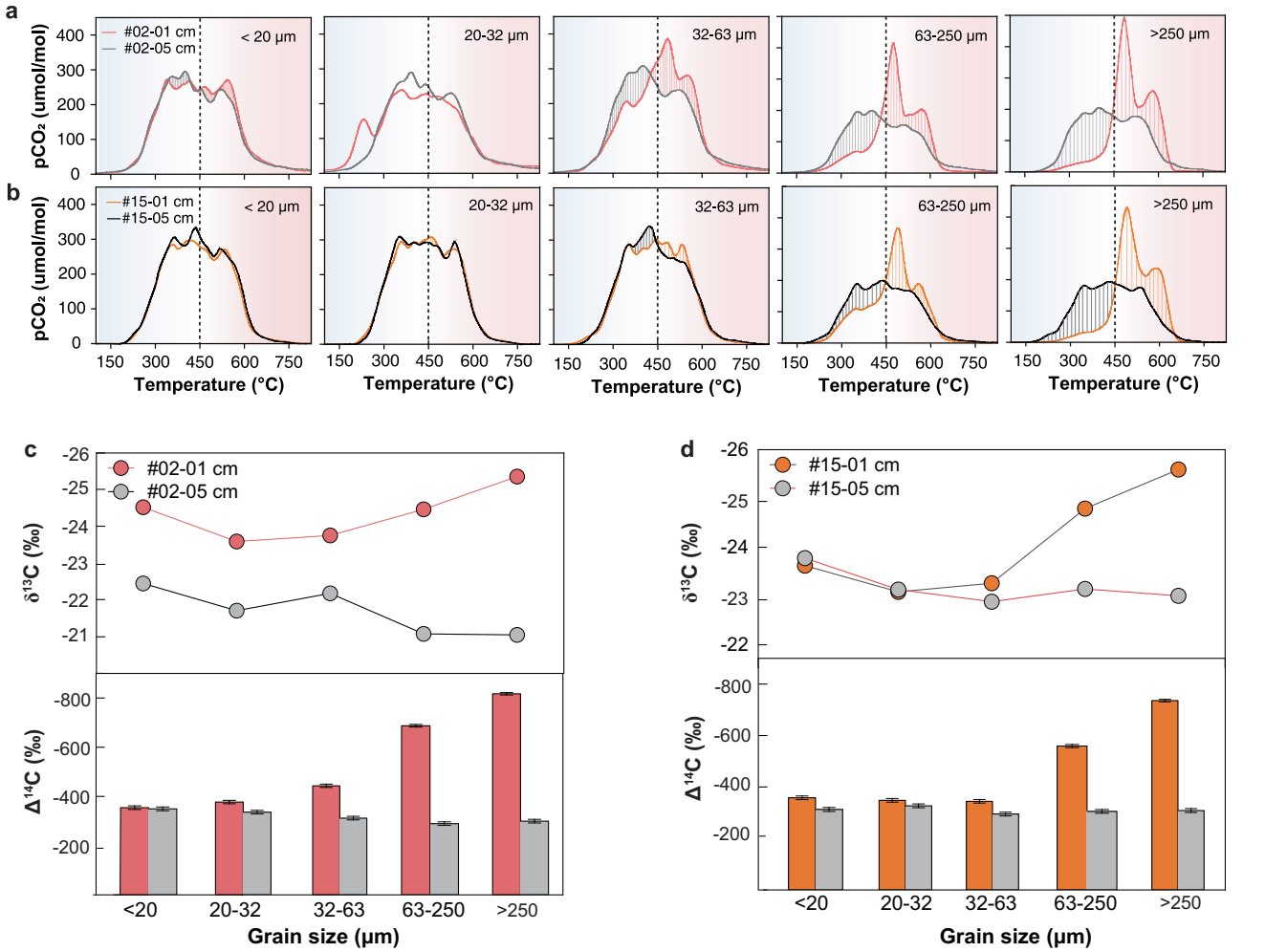


Fig. 5 | The thermal decomposition characteristics and isotopic compositions of OC across different grain-size fractions from the surface (1 cm) and deep (5 cm) sediments at active seep sites #02 and #15. a CO_2 thermograms at site #02. **b** CO_2 thermograms at site #15. **c** OC isotopic compositions at site #02. **d** OC isotopic compositions at site #15.

Within these aggregates, microbial colonization and extracellular polymeric substances may modify fine-scale aggregate morphology[29], and promote the development of complex pore networks and tortuous internal pathways[30], as illustrated by contrasting pore structures between less-colonized (Fig. 6a) and heavily colonized aggregates (Fig. 6b). These architectures physically influence solute transport within aggregates[31], thereby potentially restricting oxygen diffusion and oxidative attack, while aerobic methanotrophic activity within coarse-grained aggregates may further reduce oxygen availability, creating steep redox gradients between exterior and interior.

Superimposed on this physical occlusion, multiple complementary mechanisms may operate in concert. First, microfossil biomineral matrices—abundant in coarse fractions (Supplementary Fig. 4)—exhibit rich pore structures that increase specific surface area[32] (Fig. 6; Supplementary Fig. 5a–b), providing sorption sites for ancient, refractory methane-derived OC. Second, microbial by-products facilitate the accumulation of proteinaceous functional groups (e.g., amide and carboxylic carbon)[33], necessitating greater energy to break these bonds compared to non-methane-affected sediments. Third, microbial transformation of OC into cellular biomass may involve chemical modifications that enhance organic matter resistance to decomposition[34,35].

This multi-faceted protection mechanism is supported by OC/surface area (SA) ratios in coarse fractions, which substantially exceed the range expected from simple mineral-surface sorption models (OC loading ratios[32]: 0.4–1.0 mg C/m^2; Supplementary Fig. 5c, d). Notably, while SA does not increase from the 63–250 μm to the >250 μm fraction, OC/SA rises sharply. This decoupling implicates that pore occlusion, rather than adsorption alone, as the dominant preservation mechanism. Steep redox gradients between the aggregate exterior and interior, sustained by aerobic methanotrophic activity, reinforce the aggregates as self-protective micro-environments, enabling methane-derived OC to persist in aerobic surface sediments that would otherwise favor its oxidation. Larger aggregates with greater internal volume for such shielding correspondingly host a higher proportion of ancient OC. Collectively, these analyses establish physical occlusion within sedimentary aggregates as the important mechanism enabling methane-derived OC to persist in aerobic surface sediments—a finding that raises further questions about the long-term fate of this carbon pool during burial and diagenesis.

A methane-derived carbon sink on continental slopes

To constrain the significance of this process, we employ a two end-member model to estimate methane-derived OC contributions (See Methods). At the local scale, the active Haima cold seep in the South China Sea preserves approximately 52 t C/yr of methane-derived OC in surface sediments, which is substantially higher than in deeper sediments (11 t C/yr) and comparable to reported methane emission fluxes from the northern US Atlantic margin (11–68 t C/yr)[15]. These estimates demonstrate that methane-derived OC preservation is already a non-

https://doi.org/10.1038/s41467-026-74250-2

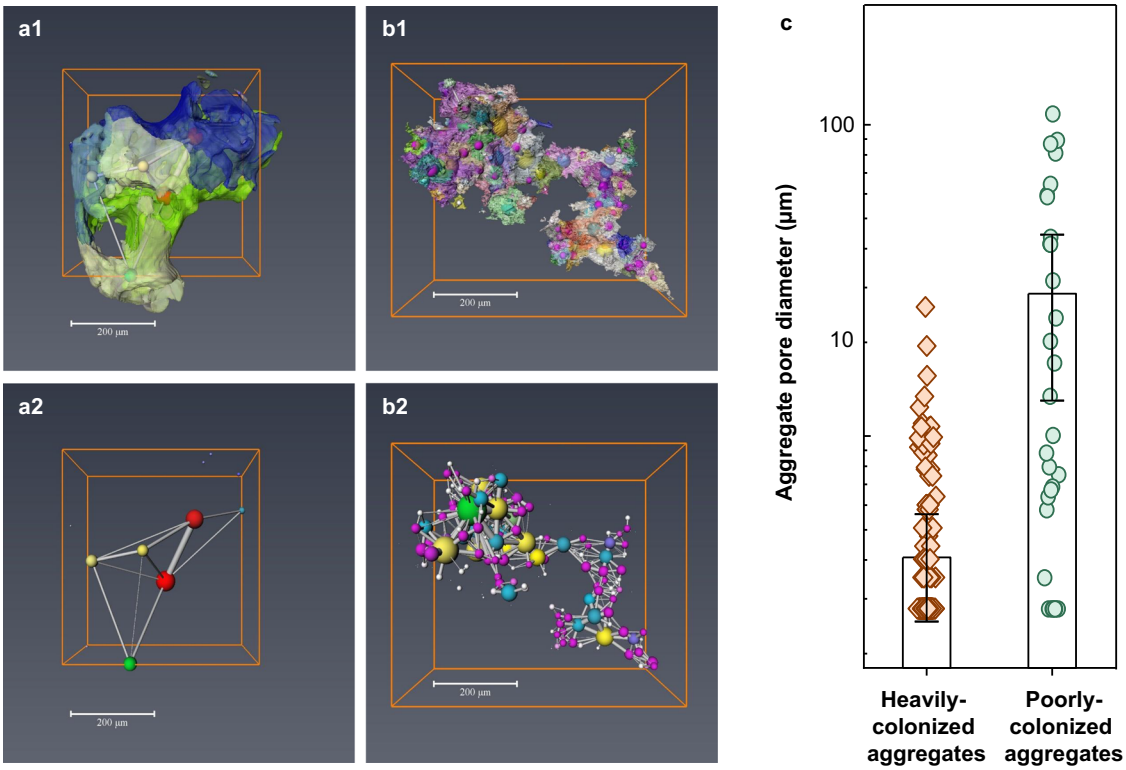


Fig. 6 | Microbial colonization progressively increases the complexity of pore networks as the volume ratio of organic matter to mineral particles rises. a1, b1 show aggregates at different microbial colonization states, with a1 representing a poorly colonized aggregate and b1 a heavily colonized aggregate. Different colors are used to distinguish individual microbe–mineral clusters within each aggregate, thereby illustrating the degree of organic matter cementation. **a2, b2** illustrate the corresponding pore networks, categorized into pores and throats, with distinct colors representing different diameter ranges. In b2, microbial colonization generates more intricate pore structures and more tortuous internal pathways relative to the less well-colonized aggregate in a2. **c** Aggregate pores in heavily (corresponding to b) and poorly (corresponding to a) colonized aggregates. The pores in heavily colonized aggregates are generally smaller than those in poorly colonized aggregates, which can restrict oxygen diffusion and oxidative degradation, thus contributing significantly to the preservation of organic matter. Each symbol represents an individual aggregate pore measurement. Bars indicate the mean, and error bars denote ±1 standard deviation.

negligible process at the scale of individual seep systems, pointing to its potentially larger role across methane-prone continental margins.

Our global synthesis demonstrates that the preservation of methane-derived OC in surface sediments is not a regional anomaly but a widespread phenomenon across diverse marine environments (Fig. 1). On global continental slopes, where vast methane hydrate reservoirs are highly susceptible to dissociation, this process reaches its quantitative peak: up to 6.1 Tg C/yr of methane-derived OC could be preserved in surface sediments. This estimate accounts for over 12.2% of the methane-derived carbon emitted from global seafloor sediments[36] and represents 1.8–4.3% of the total OC accumulation in global marine sediments[28,37]. These findings reveal that methane-derived OC preservation is not merely a localized curiosity but a quantitatively significant component of the global carbon budget.

From subsurface sequestration to surface accumulation: old methane-derived OC in deep-sea surface sediments

This preservation manifests through two fundamentally different regimes, distinguished by the depth of the SMT zone and its interplay with methane flux intensity (Fig. 7). In settings where the SMT resides at depth, representative of non- or inactive seepage systems, anaerobic oxidation of methane (AOM) drives carbonate precipitation near the SMT zone[38] and the physical encapsulation of organic matter within carbonate matrices[39]. Methane-derived OC is thus primarily sequestered at depth, with limited upward accumulation into surface sediments. Above the SMT, the OC pool is dominated by settling material from the upper water column, resulting in progressively increasing ^{14}C ages with depth toward the SMT (Fig. 7a).

In stark contrast, at active seep sites where the SMT zone shoals toward the seafloor, a fundamentally different preservation regime emerges (Fig. 7b). Here, the flux of deep-sourced methane to surface sediments increases dramatically, enabling AeOM to supplant AOM as the dominant transformation pathway near the surface sediment[40]. Aerobic methanotrophs proliferate at the sediment–water interface, secreting abundant extracellular polymeric substances that bind mineral grains, microbial cells, and organic matter into large organo-mineral aggregates. These aggregates develop complex, fine-pored, and highly tortuous internal structures that limit oxygen penetration and inhibit oxidative degradation[41], resulting in anomalously old ^{14}C ages in surface sediments (Fig. 7b)—a finding with important implications for understanding OC aging in marine environments.

Together, these processes define a continuum of methane-derived OC preservation controlled by SMT depth: from subsurface sequestration in AOM-dominated systems to surface accumulation in active seep environments driven by AeOM. In active seeps, the coupled action of AeOM, aggregate formation, internal redox zonation, and carbonate-mediated protection enables efficient transformation of deep-sourced methane into stable surface OC pools. Active seep sites thus emerge as global hotspots for methane-derived OC preservation, revealing that the sediment–water interface, rather than the deep SMT zone alone, can serve as the primary locus of methane-derived carbon burial when methane fluxes are sufficiently high (Fig. 7).

Our findings provide biogeochemical evidence that microbial fixation, chemical modification, and physical protection act in concert to promote the preservation of methane-derived OC. This mechanism has far-reaching implications: by sequestering methane-derived OC in

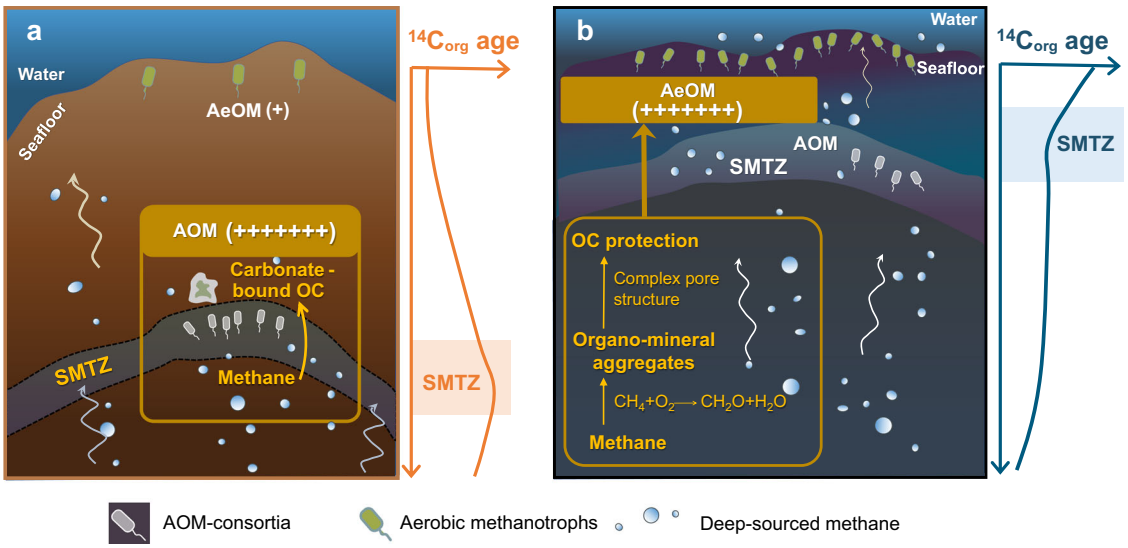


Fig. 7 | Conceptual framework illustrating the role of sulfate-methane transition zone (SMTZ) in regulating the preservation of methane-derived OC in marine sediments. a In the deeper SMTZ, methane-derived OC is primarily preserved through anaerobic oxidation of methane (AOM), driving the physical encapsulation of organic matter and carbonate-bound OC precipitation near the SMTZ, which results in progressively older OC ^{14}C ages ($^{14}C_{org}$ age) with increasing depth toward the SMTZ. **b** In the shallow SMTZ, aerobic oxidation of methane (AeOM) supplants AOM as the dominant transformation pathway near the surface sediment. The coupled action of AeOM, well-packed organo-mineral aggregates, and complex pore structure enables efficient transformation and preservation of deep-sourced methane into surface OC pools, resulting in older $^{14}C_{org}$ age in the surface sediments.

surface sediments, this preservation pathway moderates its release into the hydrosphere, thereby reducing CO_2 production from AeOM in the water column and potentially mitigating ocean acidification[42,43]. Given the ubiquitous distribution of aerobic methanotrophs in sediments, analogous transformation and preservation of microbial-mediated methane-derived OC may occur in other methane-active environments, including terrestrial wetlands[44]. While our findings demonstrate that SMT shoaling and methane-derived carbon contribute to elevated OC contents and aged $\Delta^{14}C$ signatures in surface sediments, this interpretation does not invalidate traditional views. It is well established that pre-aged terrestrial inputs and reworked marine organic matter also play roles in shaping sedimentary OC ages across many settings[19]. Nevertheless, the two mechanisms—methane-derived carbon preservation versus external supply of old carbon—are not mutually exclusive. They operate concurrently, with their relative importance varying regionally. While aged carbon from terrestrial or reworked carbon sources remains important, the key advance of our study is the discovery of a large-scale spatial control mechanism, the depth of the sulfate-methane transition zone, that subtly but significantly governs the preservation of newly generated methane-derived old carbon across global continental margins, offering a process-based explanation beyond existing views.

The efficient preservation of methane-derived OC in surface sediments thus buffers methane emissions, facilitates deep-sourced carbon burial at the sediment–water interface, and may exert a non-negligible influence on global climate regulation over geological timescales. By transforming a potent greenhouse gas into a stable sedimentary carbon pool, this previously overlooked pathway adds a dimension to our understanding of the marine carbon cycle and its feedbacks to climate change.

Methods

Sampling

During the R/V *Haiyang VI* and *Dongfanghong III* scientific expeditions in 2020 and 2022, push cores from six submarine habitats (#02, #04, #05, #06, #07, #15) were retrieved from the active Haima (16°50′ N, 110°30′ E) and Site F cold seeps (22°07′ N, 119°17′ E) located on the northern slope of the South China Sea. The cores were collected by manipulator arms of the ROV, and the submarine seepage landscapes were simultaneously observed and recorded when sampling (Fig. 2a1–f1). The sediment cores were sectioned at 1-cm intervals and then frozen at −20 °C until further processing. Sediments collected from the inner cores were stored in sterile tubes for identifying microbial gene abundance.

Sediment sieving

In order to excavate the mechanisms of methane-derived OC preservation at a higher resolution, sediments from the surface (1 cm) and deeper (5 cm) layers at active sites #02 and #15 were selected for separation and geochemical characterization analyses of different grain size fractions. The samples were dry-sieved using a Sonic Sifter Separator (Model L3P-25, Advantech Manufacturing, INC, USA) into five grain size fractions (<20, 20–32, 32–63, 63–250, and >250 μm). The fractionated samples were stored in pre-combusted (450 °C, 5 h) glass vials for analysis of OC content, $\delta^{13}C$, and $\Delta^{14}C$, and RPO.

Global data analysis

Data compilation, pre-processing of $\Delta^{14}C$ and OC content. We collected the available $\Delta^{14}C$ data and corresponding location information of marine sediments worldwide from the MOSAIC database (version 2.0)[45]. In addition, we integrated OC content data that is stored in the Pangaea[46] (Pangaea dataset DOI: 10.1594/PANGAEA.733692) and MOSAIC (version 2.0) databases[45] (Supplementary Dataset S1). We then applied preprocessing procedures to ensure the validity and reliability of the data. Firstly, we excluded records containing invalid values (e.g., non-numeric entries or OC values outside a physically reasonable range) and removed records with missing key variables (e.g., OC or water depth) to ensure the completeness and reliability of the dataset. Secondly, we selected OC content and $\Delta^{14}C$ data from depths <5 cm below the seafloor (labeled as top sediments in subsequent descriptions), as sediments in this depth range were considered to have a significant methane signature in our study. Thirdly, we selected OC content and $\Delta^{14}C$ data distributed within water depth >700 m to minimize the influence of terrestrial-sourced organic matter inputs, particularly in the context of potential methane seepage[47]. Fourthly, in cases where multiple measurements were available at a

given geographic location, we calculated the average value of these measurements to ensure only one OC content or $\Delta^{14}C$ data at each geographic location. The obtained OC content data after pre-processing included 4918 records and was presented in Supplementary Fig. 6a.

OC content prediction. In order to obtain a more comprehensive OC content distribution on a global scale, we predicted OC content using the Random Forest (RF) machine learning method. RF is an ensemble learning algorithm that constructs multiple regression trees and makes predictions by calculating the mean response across individual trees, thereby improving model stability and predictive accuracy[48]. To train the model, we collected several relevant environmental variables and examined their relationships with OC content. These variables included temperature, chlorophyll concentration, and oxygen concentration of surface seawater, water depth, salinity, and other factors (Supplementary Dataset S2), which were considered to play important roles in reflecting key characteristics of the sedimentary environment and variation of OC content[49].

To obtain a more reliable estimate of spatial predictive performance, we adopted a k-fold cross-validation strategy based on nearest neighbors using the knndm() function in the CAST package in R[50–52] among the available validation strategies[53,54]. This approach constructs spatial folds by matching the nearest-neighbor distance structure between the training–testing samples and the prediction domain, thereby providing a more realistic validation framework for spatial prediction. We optimized the model by adjusting key parameters, such as the number of trees (500) and maximum depth of trees (100), within the RF algorithm. Experimental results show that the RF model with random cross-validation achieved a prediction accuracy (R^2) of 51% on the testing sets (Supplementary Fig. 7c). The validation of the global applicability of predicted OC contents was detailed in Supplementary Text 1 and Supplementary Figs 6–9.

Estimation of SMT distribution depth. To obtain the global-scale distribution of sulfate-methane transition (SMT) depth, we estimated SMT depth based on the following empirical formula[55], which was deduced under diverse oceanic conditions globally.

$$\log(\mathrm{SMT}) = -0.92386 \times \log(\text{sedimentation rate}) - 0.48138 \quad (1)$$

The sedimentation rate used for this calculation was constructed using a depth-dependent approach. In regions with water depths of 700-2000 m, sedimentation rates were estimated using the empirical model[55], which predicted sedimentation rate from water depth, distance to coast, and sea-surface POC. In regions deeper than 2000 m, the sedimentation rate was referred from the global sedimentation-rate dataset[56], which was based on a K-nearest-neighbor (KNN) machine-learning approach trained on a large compilation of measured sediment accumulation rates. Importantly, this dataset provided per-cell uncertainty estimates, allowing us to explicitly quantify the propagation of uncertainty into SMT depth (Supplementary Fig. 10). These two components were then merged into a unified global sedimentation-rate field, which served as the basis for subsequent SMT-depth estimation.

Global distributions of OC content and SMT depth. To achieve a globally visualized distribution of OC content, we initially projected the pre-processed OC content data points onto global raster maps. A global raster map was constructed with latitude and longitude as the coordinate axes, segmenting the Earth's surface into uniform grid cells, each representing a specific spatial scale. By calculating the Euclidean distance between the measured data points and the grid network based on their latitude and longitude, we mapped the collected data points to the corresponding grid cells. Each grid cell was assigned an OC content value. In cases where a grid cell contained multiple data values, we calculated the average to determine a single valid value for that grid cell. Additionally, the predicted OC contents were simultaneously projected onto this map. This methodology effectively integrated both collected and predicted OC content data, resulting in a continuous dataset with global spatial coverage. A separate global grid map was also constructed for the estimated SMT depths. The global distribution maps for OC content and SMT depth in top marine sediments were shown (Fig. 1a–b, Supplementary Datasets S3 and S4).

To evaluate the impact of spatial resolution on our simulation results, we performed global raster projections of OC content and SMT depth at three different resolutions: 1°×1° (180×360 grids), 0.5° × 0.5° (360 × 720 grids), and 0.25° × 0.25° (720 × 1440 grids). The correlations between SMT depth and OC content were found to be remarkably consistent across all three resolutions, indicating that variations in data resolution do not affect our conclusions. Therefore, we chose the results at the highest spatial resolution to present in Fig. 1, while results at the other resolutions were included in the Supplementary Information (Supplementary Fig. 11).

Statistical analyses. To investigate the correlation between the SMT distribution depth and OC content globally, we first paired the OC content values (Fig. 1a) and SMT data (Fig. 1b) based on the same latitude and longitude information. We then divided the SMT depth at 15 m-interval within 0–400 m (Supplementary Fig. 12). Owing to the absence of matched SMT and OC data at depths greater than 405 m, the analysis between SMT depth and OC is therefore restricted to the 0-405 m depth range. We calculated the percentage of grids with higher OC content (assumed to be >1%) within each 15 m interval (Fig. 1d). Furthermore, we calculated the mean SMT distribution depth and mean OC content within each interval and fitted their relationship (Fig. 1e).

Similarly, to excavate the relationship between SMT depth and the $\Delta^{14}C$ values of OC, we first paired the SMT data and $\Delta^{14}C$ values (data from regions with water depths greater than 700 m, Supplementary Dataset S5) according to their latitude and longitude information. Given the scarcity of matched $\Delta^{14}C$ and SMT depth data pairs at depths exceeding 100 m, the analysis of SMT depth and $\Delta^{14}C$ was confined to the 0–100 m depth range. The data pairs were then grouped into 15-m intervals according to SMT depth, and the median SMT depth and $\Delta^{14}C$ value were calculated for each interval. The fitted correlation between these parameters is shown in Fig. 1f.

OC content and isotopic analysis. The pretreatment methodologies of sediments used for OC analyses were reported previously[57]. Briefly, the sediments were freeze-dried and then finely ground. Prior to organic geochemical measurements, the sediments were first acidified with 1.0 N HCl solution to remove inorganic carbon (IC) and then rinsed with Milli-Q water to remove the residual acid[22,58]. OC content and $\delta^{13}C$ were determined using an element analyzer-isotope ratio mass spectrometer (Thermo Fisher Scientific, Germany) at the Key Lab of Submarine Geosciences and Prospecting Techniques, Ocean University of China. The $\delta^{13}C$ value was reported in ‰ relative to Vienna Pee Dee Belemnite[59]. The $\delta^{13}C$ value was associated with the relative difference in the $^{13}C/^{12}C$ ratio between the sample (R_{sample}) and the standard ($R_{standard}$), which was calculated using the following equation[60]:

$$\delta^{13}C = \left(\frac{R_{sample}}{R_{standard}} - 1\right) \times 1000 \quad (2)$$

For the $\Delta^{14}C$ measurement, the homogenized and IC-removed sediments were converted to CO_2 using sealed-tube catalytic combustion. The generated CO_2 was reduced to graphite and then

analyzed by accelerator mass spectrometry (AMS) at the National Ocean Sciences Accelerator Mass Spectrometry facility (NOSAMS) of Woods Hole Oceanographic Institution (WHOI). ^{14}C abundance was reported as $\Delta^{14}C$ (‰). The measured OC contents, $\delta^{13}C$, and $\Delta^{14}C$ values were presented in Supplementary Tables 1–4.

Microbial gene abundance determination. Microbial DNA was extracted from approximately 0.5 g of fresh sediments using the E.Z.N.A. ® Soil DNA Isolation Kit (Omega Bio-tek, USA; cat. no. D5625). Microbial gene abundance was determined using real-time quantitative PCR (qPCR). The copy number of the *pmoA* functional gene was quantified using the primer pair A189f (5′-GGNGACTGGGACTTCTGG-3′) and mb661R (5′-CCGGMGCAACGTCYTTACC-3′)[61]. The copy number of the *mcrA* functional gene was quantified using the primer pair mcrA-mlas (5′-GGTGGTGTMGGDTTCACMCARTA-3′) and mcrA-rev (5′-CGTTCATBGCGTAGTTVGGRTAGT-3′)[62]. Total bacterial genes were amplified with the primer pairs of 338 F (5′-ACTCCTACGGGAGGCAG-CAG-3′) and 806 R (5′-GGACTACHVGGGTWTCTAAT-3′)[63]. Total archaeal genes were amplified using primer pairs of 524F10extF (5′-TGYCAGCCGCCGCGGTAA-3′) and Arch958RmodR (5′-YCCGGCGTT-GAVTCCAATT-3′)[64]. The qPCR reaction mixture contained 10 μL of 2× ChamQ SYBR Color qPCR Master Mix (Vazyme Biotech Co., Ltd., Nanjing, China; cat. no. Q411), 0.8 μL of each primer, 0.4 μL of 50× ROX Reference Dye 1 supplied with the kit, 2 μL of template DNA and 6 μL of ddH_2O. Thermal cycling reactions were performed as follows: a) 95 °C for 3 min; b) 40 cycles of 95 °C for 5 s, 58 °C for 30 s, and 72 °C for 1 min. All qPCR assays were conducted by Shanghai Majorbio Bio-pharm Technology Co., Ltd. (Shanghai, China), and primer sequences are provided above.

RPO coupled OC isotopic analysis. Programmed thermal decomposition was performed on sediments to separate different organic matter components based on their thermochemical stability differences. Prior to measurements, the sediments were subjected to HCl rinsing treatment to remove IC, following the detailed procedures described in the "OC content and isotopic analysis" section. Approximately 5–8 mg of IC-removed sediments were loaded into a quartz sample reactor with a quartz filter. After purging the oven with helium, the oven temperature was ramped from room temperature to 900 °C at a constant heating rate of 5 °C/min[65]. Carbonaceous organic compounds and pyrolysis products desorbed during the ramp-up process were quantitatively converted to CO_2, which was subsequently removed from the oxidizing reactor with a carrier stream of helium and measured for concentration.

To quantitatively compare the stability of organic matter across sediment samples, we calculated the E based on the evolved CO_2 thermograms as described previously[66]. This calculation selected $\omega = 10^{10}\ s^{-1}$ as the Arrhenius pre-exponential factor for all samples, and was conducted in Python programming language v.3.6 by the 'rampedpyrox' package (See reference for detailed description)[66]. Furthermore, we isolated the evolved CO_2 thermograms from surface sediment pyrolysis into three components (F1, F2, F3) using a first-order Gaussian distribution model. This method can be used to identify the composition of multi-source organic matter and was successfully applied to determine sediment sources[67].

The CO_2 thermograms from the decomposition of volatilized components in surface (1 cm) and deep (5 cm) sediments at #02 and #15 sites were integrated into five temperature windows (T1: 80 − 320 °C; T2: 320 − 391 °C; T3: 391 − 484 °C; T4: 484 − 570 °C; T5: 570 − 900 °C)[22]. The evolved CO_2 gas generated from each thermal interval was trapped for further carbon isotopic ($\delta^{13}C$ and $\Delta^{14}C$) measurements on the AMS at NOSAMS (Supplementary Table 3).

OC source apportionment. In this study, the measured OC was considered a mixture of deep-sourced, ancient methane-derived OC and background marine OC. The contribution of methane-derived carbon to OC (f_{CH4}) was calculated using the following mass balance model.

$$\Delta^{14}C_{mea} = \Delta^{14}C_{back} f_{back} + \Delta^{14}C_{CH4} f_{CH4} \quad (3)$$

$$f_{back} + f_{CH_4} = 1 \quad (4)$$

where $\Delta^{14}C_{mea}$, $\Delta^{14}C_{back}$, and $\Delta^{14}C_{CH4}$ were the $\Delta^{14}C$ values for the measured OC, background OC, and methane-derived OC, respectively. The deep-sourced methane-derived OC contained a nearly dead radioactive signature, and the $\Delta^{14}C$ end-member was assumed to be −999‰[18]. The $\Delta^{14}C$ end-member of background marine OC was estimated to be approximately −227‰ by referring to the pilot study and references therein[45,68].

Here, ^{14}C decay during sedimentation was not taken into account when calculating the source proportions (f_{CH4} and f_{back}; Supplementary Table 1). As we considered the influence of the sedimentation rate, the f_{CH4} value in the deep sediments became lower, but the f_{CH4} value in the surface layer did not change, which would also further support our statements that the surface sediments preserve more methane-derived carbon than the deeper sediments.

Methane-derived OC preservation rate in the surface sediments. The preservation rate of methane-derived OC preserved in the surface sediments can be calculated as follows:

$$\text{Methane-derived OC preservation rate} = \frac{\text{Methane} - \text{derived OC Inventory (g)}}{\text{Deposition Time (yr)}} \quad (5)$$

where methane-derived OC Inventory was the mass of methane-derived OC preserved in seepage surface sediments, and Deposition Time represented the time required for sedimentary particles to cover the top 1 cm of the uppermost sedimentary layer.

The methane-derived OC Inventory was calculated as follows:

$$\text{Methane} - \text{derived OC Inventory} = S_{dry}\,(\text{g/m}^3) \times V\,(\text{m}^3) \times \text{Methane} - \text{derived OC (\%)} \quad (6)$$

where S_{dry} represented the covering of dried sediment mass per unit volume, V was the sedimentary volume, which was the product of the distributed area in the seep region (~350 km^2 in Haima) and the assumed thickness (1 cm), and methane-derived OC (%) represented the percentage of methane-derived OC mass relative to that of the dried sediments. The averaged S_{dry} and methane-derived OC (%) in the upper 1 cm were 10.24×10^4 g/m^3 and 1.45%, respectively (Supplementary Table 5). Thus, the estimated methane-derived OC inventory within the top 1 cm sediments in the Haima seep region was ~5.2×10^3 t, which was higher than the inventory within the 5 cm sediments, ~1.1×10^3 t.

The Deposition Time (yr) was calculated by:

$$\text{Deposition Time} = \frac{\text{Thickness of Sedimentary Layer (cm)}}{\text{Deposition Rate (cm/yr)}} \quad (7)$$

The Thickness of Sedimentary Layer was determined to be 1 cm, the Deposition Rate for this region was estimated to be 0.1 mm/yr[69], and the Deposition Time was thus 100 yr. The combined results of the estimated methane-derived OC Inventory of ~5.2×10^3 t and the Deposition Time of 100 yr from Eqs. (6 and 7) obtained a preserved methane-derived OC preservation rate of ~52 t C/yr within the upper 1 cm in the Haima seep region and ~11 t C/yr within 5 cm.

To assess the global implications of methane-derived OC preservation, we quantified the preservation of methane-derived OC in surface sediments at active seeps and continental slopes worldwide. Assuming the presence of tens of thousands of active seeps covering approximately 2.05×10^4 km^2 globally[4], we estimated that around 0.003 Tg C/yr of methane-derived OC may be preserved in surface sediments at these seeps. Furthermore, given the widespread distribution of methane hydrates on continental slopes, where hydrates are prone to dissociate and release methane, we estimated that approximately 6.1 Tg C/yr of methane-derived OC may be preserved in surface sediments of the global continental slopes covering around 41 million km^2.

Three-dimensional (3D) structure acquisition and pore network quantification. The three-dimensional (3D) internal structures of organo–mineral aggregates were characterized using X-ray micro-computed tomography (micro-CT), following previously established procedures for sample collection, wet preservation, scanning, and image analysis[29,70]. Two representative organomineral aggregates that were collected from surface sediments in the Tay estuary, Scotland, were represented herein[29]. To preserve the hydrated internal architecture and minimize structural artefacts associated with dehydration, resin embedding or drying, we applied wet-scanning aggregates adapted from previous work[70]. Prior to scanning, individual aggregates from marine surface sediments were isolated and transferred into sealed containers suitable for wet micro-CT imaging[29]. Scans were acquired at a voxel size of 0.8 × 0.8 × 0.8 μm^3, which enabled submicron-scale visualization of aggregate interiors, including mineral particles, organic-rich domains, and internal pore space. Raw projection data were reconstructed into 3D image stacks using the standard reconstruction workflow[70]. The reconstructed volumes were then cropped to retain the target aggregate and processed for phase segmentation, allowing the distinction of aggregate solids from pore space in 3D.

Pore networks were subsequently extracted and quantified following the protocols detailed in Lawrence et al.[71]. Pore networks were classified into pores and throats using a skeletonization algorithm[72], in which individual pore segments were identified from the skeleton, and throats were defined as the connections between adjacent pores. The analysis was performed directly on intact 3D volumes; it thus preserved the spatial relationships between pore domains and surrounding organo–mineral matrices, thereby providing a mechanistic basis for evaluating physical protection of organic matter within aggregate interiors.

Data availability

The datasets generated and analysed in this study are provided in the Supplementary Information and Source Data file. They are also available from the Figshare repository at https://doi.org/10.6084/m9.figshare.32385312. Source data are provided with this paper.

Code availability

The code generated and used for data processing, analysis, and visualization in this study is available from the Figshare repository at https://doi.org/10.6084/m9.figshare.32385312.

References

1. Saunois, M. et al. The global methane budget 2000–2017. *Earth Syst. Sci. Data* **12**, 1561–1623 (2020).
2. Ruppel, C. D. & Kessler, J. D. The interaction of climate change and methane hydrates. *Rev. Geophys.* **55**, 126–168 (2017).
3. Kretschmer, K., Biastoch, A., Rüpke, L. & Burwicz, E. Modeling the fate of methane hydrates under global warming. *Glob. Biogeochem. Cycles* **29**, 610–625 (2015).
4. Boetius, A. & Wenzhöfer, F. Seafloor oxygen consumption fuelled by methane from cold seeps. *Nat. Geosci.* **6**, 725–734 (2013).
5. Schuur, E. A. G. et al. Climate change and the permafrost carbon feedback. *Nature* **520**, 171–179 (2015).
6. Milkov, A. V., Sassen, R., Apanasovich, T. V. & Dadashev, F. G. Global gas flux from mud volcanoes: A significant source of fossil methane in the atmosphere and the ocean. *Geophys. Res. Lett.* **30**, 1037 (2003).
7. Cao, L. et al. In situ detection of the fine scale heterogeneity of active cold seep environment of the Formosa Ridge, the South China Sea. *J. Mar. Syst.* **218**, 103530 (2021).
8. Panieri, G. et al. An integrated view of the methane system in the pockmarks at Vestnesa Ridge, 79° *N. Mar. Geol.* **390**, 282–300 (2017).
9. Boetius, A. et al. A marine microbial consortium apparently mediating anaerobic oxidation of methane. *Nature* **407**, 623–626 (2000).
10. Knittel, K. & Boetius, A. Anaerobic oxidation of methane: progress with an unknown process. *Annu. Rev. Microbiol.* **63**, 311–334 (2009).
11. Yang, S. et al. Genomic and enzymatic evidence of acetogenesis by anaerobic methanotrophic archaea. *Nat. Commun.* **11**, 3941 (2020).
12. Bhatnagar, G., Chapman, W. G., Dickens, G. R., Dugan, B. & Hirasaki, G. J. Sulfate-methane transition as a proxy for average methane hydrate saturation in marine sediments. *Geophys. Res. Lett.* **35**, L03611 (2008).
13. Lapham, L. L. et al. Methane leakage through the sulfate–methane transition zone of the Baltic seabed. *Nat. Geosci.* **17**, 1277–1283 (2024).
14. Wei, J. et al. Seafloor methane emission on the Makran continental margin. *Sci. Total Environ.* **801**, 149772 (2021).
15. Skarke, A., Ruppel, C., Kodis, M., Brothers, D. & Lobecker, E. Widespread methane leakage from the sea floor on the northern US Atlantic margin. *Nat. Geosci.* **7**, 657–661 (2014).
16. Feng, D. et al. Cold seep systems in the South China Sea: An overview. *J. Asian Earth Sci.* **168**, 3–16 (2018).
17. Zhang, X. et al. In situ Raman detection of gas hydrates exposed on the seafloor of the South China Sea. *Geochem. Geophys. Geosyst.* **18**, 3700–3713 (2017).
18. Pohlman, J. W. et al. Methane sources in gas hydrate-bearing cold seeps: Evidence from radiocarbon and stable isotopes. *Mar. Chem.* **115**, 102–109 (2009).
19. Griffith, D. R., Martin, W. R. & Eglinton, T. I. The radiocarbon age of organic carbon in marine surface sediments. *Geochim. Cosmochim. Acta* **74**, 6788–6800 (2010).
20. Blattmann, T. M. et al. Contrasting fates of petrogenic and biospheric carbon in the South China Sea. *Geophys. Res. Lett.* **45**, 9077–9086 (2018).
21. DeMaster, D. J., Taylor, R. S., Smith, C. R., Isla, E. & Thomas, C. J. Using radiocarbon to assess the abundance, distribution, and nature of labile organic carbon in marine sediments. *Glob. Biogeochem. Cycles* **35**, e2020GB006676 (2021).
22. Bao, R., McNichol, A. P., Hemingway, J. D., Lardie Gaylord, M. C. & Eglinton, T. I. Influence of different acid treatments on the radiocarbon content spectrum of sedimentary organic matter determined by RPO/Accelerator Mass Spectrometry. *Radiocarbon* **61**, 395–413 (2019).
23. Hemingway, J. D. et al. Mineral protection regulates long-term global preservation of natural organic carbon. *Nature* **570**, 228–231 (2019).
24. Marin-Spiotta, E. et al. Long-term stabilization of deep soil carbon by fire and burial during early Holocene climate change. *Nat. Geosci.* **7**, 428–432 (2014).
25. Ge, T., Xue, Y., Jiang, X., Zou, L. & Wang, X. Sources and radiocarbon ages of organic carbon in different grain size fractions of Yellow River-transported particles and coastal sediments. *Chem. Geol.* **534**, 119452 (2020).

26. Michaud, A. B. et al. Microbial oxidation as a methane sink beneath the West Antarctic Ice Sheet. *Nat. Geosci.* **10**, 582–586 (2017).
27. He, R., Wooller, M. J., Pohlman, J. W., Tiedje, J. M. & Leigh, M. B. Methane-derived carbon flow through microbial communities in arctic lake sediments. *Environ. Microbiol.* **17**, 3233–3250 (2015).
28. Wallmann, K. et al. The global inventory of methane hydrate in marine sediments: a theoretical approach. *Energies* **5**, 2449–2498 (2012).
29. Zhang, N. et al. Drag acting on suspended sediment increased by microbial colonization. *Nat. Geosci.* **18**, 396–401 (2025).
30. Kravchenko, A. N. & Guber, A. K. Soil pores and their contributions to soil carbon processes. *Geoderma* **287**, 31–39 (2017).
31. Zetsche, E.-M., Larsson, A. I., Iversen, M. H. & Ploug, H. Flow and diffusion around and within diatom aggregates: Effects of aggregate composition and shape. *Limnol. Oceanogr.* **65**, 1818–1833 (2020).
32. Blair, N. E. & Aller, R. C. The fate of terrestrial organic carbon in the marine environment. *Annu. Rev. Mar. Sci.* **4**, 401–423 (2012).
33. Estes, E. R. et al. Persistent organic matter in oxic subseafloor sediment. *Nat. Geosci.* **12**, 126–131 (2019).
34. Schillawski, S. & Petsch, S. Release of biodegradable dissolved organic matter from ancient sedimentary rocks. *Glob. Biogeochem. Cycles* **22**, GB3002 (2008).
35. Petsch, S. T., Eglinton, T. I. & Edwards, K. J. ^{14}C-dead living biomass: Evidence for microbial assimilation of ancient organic carbon during shale weathering. *Science* **292**, 1127–1131 (2001).
36. Kvenvolden, K. A., Lorenson, T. D. & Reeburgh, W. S. Attention turns to naturally occurring methane seepage. *Eos Trans. Am. Geophys. Union* **82**, 457 (2001).
37. Keil, R. Anthropogenic forcing of carbonate and organic carbon preservation in marine sediments. *Annu. Rev. Mar. Sci.* **9**, 151–172 (2017).
38. Xu, S., Liu, B., Wu, Z., Kowalski, N. & Böttcher, M. E. The role of anaerobic methane oxidation on the carbonate authigenesis in sediments of the subtropical Beibu Gulf, South China Sea: A reactive–transport modelling approach. *Chem. Geol.* **619**, 121319 (2023).
39. Feng, D. et al. Contribution of deep-sourced carbon from hydrocarbon seeps to sedimentary organic carbon: Evidence from radiocarbon and stable isotope geochemistry. *Chem. Geol.* **585**, 120572 (2021).
40. Pohlman, J. W. et al. Anaerobic methane oxidation in low-organic content methane seep sediments. *Geochim. Cosmochim. Acta* **108**, 184–201 (2013).
41. Ploug, H. & Bergkvist, J. Oxygen diffusion limitation and ammonium production within sinking diatom aggregates under hypoxic and anoxic conditions. *Mar. Chem.* **176**, 142–149 (2015).
42. Garcia-Tigreros, F. et al. Estimating the impact of seep methane oxidation on ocean pH and dissolved inorganic radiocarbon along the U.S. mid-Atlantic bight. *J. Geophys. Res. Biogeosci.* **126**, e2019JG005621 (2021).
43. Kessler, J. D. et al. A persistent oxygen anomaly reveals the fate of spilled methane in the deep Gulf of Mexico. *Science* **331**, 312–315 (2011).
44. Simpkins, G. Methane from wetlands. *Nat. Rev. Earth Environ.* **2**, 162 (2021).
45. Paradis, S. et al. The modern ocean sediment archive and inventory of carbon (MOSAIC): version 2.0. *Earth Syst. Sci. Data* **15**, 4105–4125 (2023).
46. Seiter, K., Hensen, C., Schröter, J. & Zabel, M. Organic carbon content in surface sediments—defining regional provinces. *Deep. Res. Part I Oceanogr. Res. Pap.* **51**, 2001–2026 (2004).
47. Davies, R. J. et al. Long-distance migration and venting of methane from the base of the hydrate stability zone. *Nat. Geosci.* **17**, 32–37 (2024).
48. Wang, C. et al. Global patterns of organic carbon transfer and accumulation across the land–ocean continuum constrained by radiocarbon data. *Nat. Geosci.* **17**, 778–786 (2024).
49. Paradis, S. et al. Unraveling environmental forces shaping surface sediment geochemical "Isodrapes" in the east Asian marginal seas. *Glob. Biogeochem. Cycles* **38**, e2023GB007839 (2024).
50. Linnenbrink, J., Milà, C., Ludwig, M. & Meyer, H. kNNDM CV: k-fold nearest-neighbour distance matching cross-validation for map accuracy estimation. *Geosci. Model Dev.* **17**, 5897–5912 (2024).
51. Meyer, H. & Pebesma, E. Predicting into unknown space? Estimating the area of applicability of spatial prediction models. *Methods Ecol. Evol.* **12**, 1620–1633 (2021).
52. Meyer, H. & Pebesma, E. Machine learning-based global maps of ecological variables and the challenge of assessing them. *Nat. Commun.* **13**, 2208 (2022).
53. Valavi, R., Elith, J., Lahoz-Monfort, J. J. & Guillera-Arroita, G. blockCV: an R package for generating spatially or environmentally separated folds for k-fold cross-validation of species distribution models. *Methods Ecol. Evol.* **10**, 225–232 (2019).
54. Ploton, P. et al. Spatial validation reveals poor predictive performance of large-scale ecological mapping models. *Nat. Commun.* **11**, 4540 (2020).
55. Egger, M., Riedinger, N., Mogollón, J. M. & Jørgensen, B. B. Global diffusive fluxes of methane in marine sediments. *Nat. Geosci.* **11**, 421–425 (2018).
56. Restreppo, G. A., Wood, W. T. & Phrampus, B. J. Oceanic sediment accumulation rates predicted via machine learning algorithm: towards sediment characterization on a global scale. *Geo-Mar. Lett.* **40**, 755–763 (2020).
57. Bao, R. et al. Widespread dispersal and aging of organic carbon in shallow marginal seas. *Geology* **44**, 791–794 (2016).
58. Bao, R., Blattmann, T. M., McIntyre, C., Zhao, M. & Eglinton, T. I. Relationships between grain size and organic carbon 14C heterogeneity in continental margin sediments. *Earth Planet. Sci. Lett.* **505**, 76–85 (2019).
59. Ding, L. et al. Radiocarbon in dissolved organic and inorganic carbon of the South China Sea. *J. Geophys. Res. Ocean* **125**, e2020JC016073 (2020).
60. McNichol, A. P. & Aluwihare, L. I. The power of radiocarbon in biogeochemical studies of the marine carbon cycle: insights from studies of dissolved and particulate organic carbon (DOC and POC). *Chem. Rev.* **107**, 443–466 (2007).
61. Deng, Y., Liu, Y., Dumont, M. & Conrad, R. Salinity affects the composition of the aerobic methanotroph community in alkaline lake sediments from the Tibetan Plateau. *Microb. Ecol.* **73**, 101–110 (2017).
62. Steinberg, L. M. & Regan, J. M. *mcrA*-targeted real-time quantitative PCR method to examine methanogen communities. *Appl. Environ. Microbiol.* **75**, 4435–4442 (2009).
63. Xu, N., Tan, G. C., Wang, H. Y. & Gai, X. P. Effect of biochar additions to soil on nitrogen leaching, microbial biomass and bacterial community structure. *Eur. J. Soil Biol.* **74**, 1–8 (2016).
64. Liu, C., Li, H., Zhang, Y., Si, D. & Chen, Q. Evolution of microbial community along with increasing solid concentration during high-solids anaerobic digestion of sewage sludge. *Bioresour. Technol.* **216**, 87–94 (2016).
65. Wu, W. et al. An approach for carbon content measurement in marine sediment: Application of organic and elemental carbon analyzer. *Mar. Environ. Res.* **188**, 106000 (2023).
66. Hemingway, J. D., Rothman, D. H., Rosengard, S. Z. & Galy, V. V. Technical note: an inverse method to relate organic carbon reactivity to isotope composition from serial oxidation. *Biogeosciences* **14**, 5099–5114 (2017).

67. Rosenheim, B. E. & Galy, V. Direct measurement of riverine particulate organic carbon age structure. *Geophys. Res. Lett.* **39**, L19703 (2012).
68. Zhang, J. et al. Carbon isotopic constraints on basin-scale vertical and lateral particulate organic carbon dynamics in the northern South China Sea. *J. Geophys. Res. Ocean* **127**, e2022JC018830 (2022).
69. Liu, S., Feng, X., Feng, Z., Xiao, X. & Feng, L. Geochemical evidence of methane seepage in the sediments of the Qiongdongnan Basin, South China Sea. *Chem. Geol.* **543**, 119588 (2020).
70. Zhang, N. et al. Nondestructive 3D imaging and quantification of hydrated biofilm-sediment aggregates using X-ray microcomputed tomography. *Environ. Sci. Technol.* **52**, 13306–13313 (2018).
71. Lawrence, T. J., Carr, S. J., Wheatland, J. A. T., Manning, A. J. & Spencer, K. L. Quantifying the 3D structure and function of porosity and pore space in natural sediment flocs. *J. Soils Sediments* **22**, 3176–3188 (2022).
72. Youssef, S. et al. High resolution CT and pore-network models to assess petrophysical properties of homogeneous and heterogeneous carbonates. In SPE/EAGE Reservoir Characterization and Simulation Conference, Abu Dhabi, UAE, 28–31 October 2007, SPE-111427-MS (2007).

Acknowledgements

Data and samples were collected onboard R/V *Haiyang VI*, organized by Guangzhou Marine Geological Survey, and R/V *Dongfanghong 3*, implementing the open research cruise. We thank all crews for their assistance in collecting sediment and water samples. We also greatly appreciate the assistance of staff from NOSAMS and Ocean University of China in all aspects of the carbon isotopic measurements. We are also grateful to John D. Kessler, Jack Middelburg, and Donald E. Canfield for their constructive comments on this manuscript.

Author contributions

R.B. designed the study. Y.C., M.L., and N.Z. conducted sample measurements. Y.Z. and Z.C. provided the samples. Y.C., M.L., N.Z., L.D., and S.L. drafted figures. R.B., Y.C., M.L., N.Z., Y.Z. and L.D. wrote the original manuscript. R.B., Y.C., M.L., N.Z., Y.Z., L.D., S.L., O.A.S., M.Y., Z.C., S.Y., N.W., L.Z., J.C., M.B., H.L., L.C., W.W., H.M., and D.J.B. contributed to the review of this manuscript.

Funding

This research is supported by the National Natural Science Foundation of China (NSFC 42525604), the National Key R&D Program of China (2025YFF0516900 & 2025YFF0516903), NSFC (42450135, 92058207), and the Special Project for Introduced Talents Team of Southern Marine Science and Engineering Guangdong Laboratory (GML2019ZD0209). The open research cruise NORC2021-582 is supported by the NSFC Shiptime Sharing Project (42049582).

Competing interests

The authors declare no competing interests.

Additional information

Supplementary information The online version contains supplementary material available at https://doi.org/10.1038/s41467-026-74250-2.

Correspondence and requests for materials should be addressed to Rui Bao.

Peer review information *Nature Communications* thanks Markus Diesing, Bin Zhao and the other, anonymous, reviewer(s) for their contribution to the peer review of this work. A peer review file is available.

Reprints and permissions information is available at http://www.nature.com/reprints

Publisher's note Springer Nature remains neutral with regard to jurisdictional claims in published maps and institutional affiliations.

Open Access This article is licensed under a Creative Commons Attribution-NonCommercial-NoDerivatives 4.0 International License, which permits any non-commercial use, sharing, distribution and reproduction in any medium or format, as long as you give appropriate credit to the original author(s) and the source, provide a link to the Creative Commons licence, and indicate if you modified the licensed material. You do not have permission under this licence to share adapted material derived from this article or parts of it. The images or other third party material in this article are included in the article's Creative Commons licence, unless indicated otherwise in a credit line to the material. If material is not included in the article's Creative Commons licence and your intended use is not permitted by statutory regulation or exceeds the permitted use, you will need to obtain permission directly from the copyright holder. To view a copy of this licence, visit http://creativecommons.org/licenses/by-nc-nd/4.0/.

© The Author(s) 2026